



UNIVERSITÀ
DEGLI STUDI
FIRENZE

FLORE

Repository istituzionale dell'Università degli Studi di Firenze

Analysis of Inertial Measurement Units Performances Under Dynamic Conditions

Questa è la Versione finale referata (Post print/Accepted manuscript) della seguente pubblicazione:

Original Citation:

Analysis of Inertial Measurement Units Performances Under Dynamic Conditions / Patrizi G.; Carratu M.; Ciani L.; Sommella P.; Catelani M.; Pietrosanto A.. - In: IEEE TRANSACTIONS ON INSTRUMENTATION AND MEASUREMENT. - ISSN 0018-9456. - ELETTRONICO. - 72:(2023), pp. 3520713.1-3520713.13. [10.1109/TIM.2023.3284957]

Availability:

The webpage <https://hdl.handle.net/2158/1341691> of the repository was last updated on 2023-10-31T14:11:48Z

Published version:

DOI: 10.1109/TIM.2023.3284957

Terms of use:

Open Access

La pubblicazione è resa disponibile sotto le norme e i termini della licenza di deposito, secondo quanto stabilito dalla Policy per l'accesso aperto dell'Università degli Studi di Firenze (<https://www.sba.unifi.it/upload/policy-oa-2016-1.pdf>)

Publisher copyright claim:

Conformità alle politiche dell'editore / Compliance to publisher's policies

Questa versione della pubblicazione è conforme a quanto richiesto dalle politiche dell'editore in materia di copyright.

This version of the publication conforms to the publisher's copyright policies.

La data sopra indicata si riferisce all'ultimo aggiornamento della scheda del Repository FloRe - The above-mentioned date refers to the last update of the record in the Institutional Repository FloRe

(Article begins on next page)

Analysis of Inertial Measurement Units Performances Under Dynamic Conditions

Gabriele Patrizi^{ID}, *Member, IEEE*, Marco Carratù^{ID}, *Member, IEEE*, Lorenzo Ciani^{ID}, *Senior Member, IEEE*, Paolo Sommella^{ID}, *Member, IEEE*, Marcantonio Catelani^{ID}, *Member, IEEE*, and Antonio Pietrosanto^{ID}, *Senior Member, IEEE*

Abstract—Inertial measurement units (IMUs) are nowadays widespread in the automotive industry. Micro-electromechanical systems (MEMS) IMUs are expanding because of several advantages of this technology. However, a significant research gap neglected by both manufacturers and recent literature regards the behavior of their performances under dynamic conditions and operating under harsh environments. Before the actual installation on the field, the performances of such devices in the presence of vibration sources and mechanical load stresses must be investigated. Trying to fill this gap, this article investigates the behavior of MEMS-based IMU under dynamic conditions and random vibration tests. The proposed experimental platform also includes a specific device used to generate repeatable, controlled movement, ensuring a dynamic characterization. The analysis consists of both time and frequency domains, with specific metrics defined to evaluate the negative effects of harsh conditions on IMU performances. The results aim to highlight the limitation of the device under test when used in the automotive industry, i.e., in the presence of significant vibration noise.

Index Terms—Accelerometers, gyroscopes, inertial navigation, metrology, testing.

I. INTRODUCTION

INDUSTRY 4.0 is currently representing an important revolution in many manufacturing and technological fields. Such a process is strongly pushing toward developing and installing several different kinds of sensors [1], [2]. All these sensors are used to rapidly and accurately acquire a large amount of data for real-time decision-making in the context of diagnostic and prognostic, maintainability, optimization, and control [3], [4]. Moreover, in many industrial fields, the adequate use of specific sensors can remarkably improve the estimation of remaining useful life and the management of condition-based maintenance. Consequently, system downtime can be minimized with considerable savings in terms of money and resources.

Manuscript received 3 May 2023; accepted 29 May 2023. Date of publication 9 June 2023; date of current version 26 June 2023. The Associate Editor coordinating the review process was Dr. Lihui Peng. (*Corresponding author: Lorenzo Ciani.*)

Gabriele Patrizi, Lorenzo Ciani, and Marcantonio Catelani are with the Department of Information Engineering, University of Florence, 50139 Florence, Italy (e-mail: gabriele.patrizi@unifi.it; lorenzo.ciani@unifi.it; marcantonio.catelani@unifi.it).

Marco Carratù, Paolo Sommella, and Antonio Pietrosanto are with the Department of Industrial Engineering, University of Salerno, 84084 Fisciano, Italy (e-mail: mcarratu@unisa.it; psommella@unisa.it; apietrosanto@unisa.it). Digital Object Identifier 10.1109/TIM.2023.3284957

Nowadays, one of the industrial sectors leading toward this transformation is the automotive industry [5], [6]. Highly specialized products such as self-driving vehicles, electric propulsion-based vehicles, racing vehicles, and intelligent vehicles require many signals to be acquired and analyzed to achieve optimal performances. In this point of view, several sensors can be implemented in motorcycles and cars for the optimization of control strategy, as well as for condition monitoring and diagnostics [7], [8], [9].

Among all different types of sensing devices, inertial measurement units (IMUs) are quite commonly installed in vehicles to obtain data about real-time positioning [10], [11]. In order to do that, IMUs are complex items integrating more than one “subsensors” in the same package. The most common are triaxial gyroscopes and triaxial accelerometers, but also other sensing devices can be integrated, such as magnetometers or thermal transducers. In order to integrate more than one sensor in a single small package, micro-electromechanical systems (MEMS) is the optimal choice to achieve an outstanding tradeoff in terms of dimension and weight, power consumption, metrological performances, and cost [12], [13]. When such sensors are used in a mission-critical object (i.e., a self-driving vehicle), in an explosion risk environment (i.e., a battery-powered vehicle), or in a top-performance highly stressed vehicle (i.e., racing cars or racing motorcycles), the metrological performances of the MEMS-based IMU become of significant importance. Piezoelectric materials represent an alternative technology for IMU. The use of piezoelectric inertial sensors ensures higher performances in terms of accuracy, resolution, and stability. However, designers’ choices are mostly still toward the MEMS-based IMU because of dimension and weight constraints. As a consequence, it is becoming of crucial and fundamental importance the investigation of the metrological characteristics and reliability of MEMS-based IMUs. Proper metrological and reliability parameters are essential in order to ensure adequate system response in harsh environments during the entire system life cycle [14].

Most of the time, manufacturers miss extensively considering the characterization of IMUs in the case of external stress sources. However, in many practical application fields, the operating conditions could be highly harsh regarding mechanical, thermal, or electrical stresses. In the case of automotive applications, one of the most critical environmental

conditions that must be carefully considered is related to mechanical loads. According to several international standards and test reports, random vibration sources could affect the performances of electronic devices mounted in cars, trucks, and motorcycles [15], [16]. The nature of this vibration in terms of magnitude and frequency could vary remarkably depending on the electronic device's type and place of installation. A detailed review and discussion about this kind of external vibration stress in the automotive field have already been published in [17].

A suitable analysis of the sensor under stressed conditions is required to ensure that the considered MEMS-based IMUs will work properly after the installation on a real operating context [18], [19]. However, most of the works found in the literature are based on a static test performed under nominal conditions. For instance, the characterization of a microplatform composed of a triaxial accelerometer and a triaxial gyroscope under nominal conditions is presented in [20].

In [21], a characterization and calibration procedure based on the rate table test and tumble test is presented for gyroscopes and accelerometers, respectively. Similarly, a measurement setup for evaluating sensitivity for a differential capacitive MEMS accelerometer is presented in [22], while steady-state vibration and random acceleration are used to characterize tactical grade IMU in [23].

In some previous studies, we proposed the analysis of MEMS-based IMU performances under vibration and temperature stresses and static conditions [24], [25], [26]. The proposed works aimed at analyzing the performances of the device considering the real scenario in which the system will be installed. Only a few similar characterizations have been found in the literature concerning testing-cost MEMS-based IMU under temperature, time, and G-level [27] or regarding the vibration test of wearable IMU devices [28]. The investigations mentioned above have been carried out considering the mechanical and thermal loads endured by the IMUs when installed in terrestrial vehicles. It is important to note that our previous studies and all the previously published articles found in the literature consider analyses only in static conditions. This means that the device was kept on hold in a fixed position in the previous tests while subjected to external stress stimuli (either vibration or temperature). The preliminary static analysis allowed us to investigate, study, and metrologically describe the cross-axis sensitivity, the transfer function of the sensor, the spurious response, the sensor's antialiasing filter, the signal-to-noise ratio, the temperature drift, and temperature dependence.

Thus, this work aims to investigate the inertial platform performances under dynamic conditions, typical of a realistic scenario like the automotive field. More in detail, the objective of this article is to study and analyze the IMU's response and the ability to precisely acquire a specific repeatable movement in the presence of a random noise source that well describes a realistic installation in a terrestrial vehicle (e.g., cars, trucks, or motorcycles). In order to achieve these purposes, a customized experimental setup has been developed with the aim of exciting the device under test with two simultaneous stimuli, namely, a realistic low-frequency movement toward

two rotational axes, and a high-frequency random noise that emulates all possible vibration noise sources that can be found in automotive applications.

The IMU's response has been analyzed both qualitatively on the acquired signal and quantitatively with the introduction of dedicated metrics in both time and frequency domains.

The proposed experimental platform and the combination of both time- and frequency-domain analyses allowed investigating, in advance, all the possible issues and faulty behavior of the device when it is subjected to the actual operating conditions and before the actual installation in the automotive field.

A summary of the major contributions brought by this article is as follows.

- 1) Development of a specific experimental platform for IMUs performance analysis under dynamic operating conditions typical of automotive applications.
- 2) Investigation of the actual IMU's response during a repeatable movement while subjected to external sources of stress and noise.
- 3) Time-domain analysis for introducing specific metrics to characterize performances of the IMU subjected to external stimuli under dynamic conditions.
- 4) Frequency-domain analysis for evaluating a noise level to be used as a ground level in automotive applications.

II. PROPOSED TESTING PROCEDURES FOR DYNAMIC CHARACTERIZATION OF INERTIAL UNITS

Two external stimuli are required to implement an experimental analysis of an inertial platform under dynamic conditions. First of all, it is essential to guarantee an automatic, reproducible, and controllable movement. This stimulus is based on a set of simple low-frequency spectral components that simulate the vehicle's actual movement in which the inertial platform shall be installed.

Furthermore, it is necessary to generate the external conditions typical of the automotive field of application. In this work, only external mechanical loads are taken into consideration. However, this study could be extended to include other stresses typical of automotive fields (such as temperature and pressure). More in detail, the IMU is forced to endure a wideband random vibration that emulates the high-frequency Gaussian noise always present in terrestrial vehicles.

In compliance with the international standard ISO 16750-3 [29] published by the International Organization for Standardization, electronic devices mounted on motorcycles, trucks, and automobiles are usually subjected to high-frequency random vibration noise. The causes of such vibration noise could be manyfold, such as the engine working, some sudden movements of the suspensions, the intake air, the natural mechanical frictions between gears, or simply caused by the many irregularities of the street surface. There are also other standards published by international organizations such as the International Electrotechnical Commission (see [30]), the Automotive Electronics Council (see AEC-Q100-revH [31]), and the European Telecommunications Standards Institute (see ETSI EN 300 019-2-5 [32]) that agrees with the ISO 16750-3 [29] about the presence of such random noise.

According to the standards mentioned above, the vibration noise that electronic, microelectronic, and Internet of Things (IoT) devices must endure on terrestrial vehicles depends on the type of vehicle (either a motorcycle, a car, or a truck) and the type of installation (e.g., a device mounted on the engine, mounted on the gearbox, and installed on the suspension or directly on the vehicle's chassis). However, in all cases, the vibration experienced by the devices is a random combination of Gaussian components with different amplitudes and frequencies. The vehicle type and installation influence the G-level of the spectral components and the excitation band, which is almost always limited within the range from 200 Hz to 1 kHz [29]. Only a few exceptional causes could lead to vibration noise in a higher frequency range; thus, they have been neglected in this work.

The most suitable type of vibration test for the emulation of the automotive operating condition is the random vibration test, as in [30]. In this type of experiment, multiple Gaussian stimuli, characterized by different excitation frequencies, are simultaneously applied to the device under test. The severity of the test plan is thus provided using the acceleration spectral density (ASD) over the considered frequency range.

The actual operating conditions in this work have been simulated considering four vibration conditions, as detailed in the following.

- 1) **NOISE (A):** It is characterized by a constant ASD equal to $0.01 \text{ g}^2/\text{Hz} = 1 \text{ m}^2/\text{s}^3$. The wideband random vibration that makes up this operating condition is uniformly distributed in the lower part of the considered bandwidth, between 200 and 500 Hz.
- 2) **NOISE (B):** This operating condition can be considered complementary to the previous case. A constant wideband random vibration with $\text{ASD} = 0.01 \text{ g}^2/\text{Hz}$ is uniformly distributed within the 500 Hz ÷ 1000-Hz bandwidth.
- 3) **NOISE (C):** This stress represents the most severe operating conditions, where a wideband random vibration noise is applied in the entire considered bandwidth, between 200 Hz and 1 kHz. For the sake of comparison with the previous cases, the spectral acceleration density is maintained constant and equal to $\text{ASD} = 0.01 \text{ g}^2/\text{Hz}$.
- 4) **REFERENCE (NO NOISE):** In this case, no random vibration noise is applied. This operating profile is used as a reference condition in order to compare the performances of the IMU under test when external stresses typical of the automotive field are applied or not. This comparison allows investigating and quantifying the effects that the actual stresses induced in the performances of the device.

The random vibration profiles described above and used to emulate different automotive operating conditions are illustrated in Fig. 1.

It is important to note that the proposed noise conditions are uncorrelated with any kind of movements that the device should measure and register.

The vibration noise is applied by a dedicated device only to simulate the real condition experienced in terrestrial vehicles.

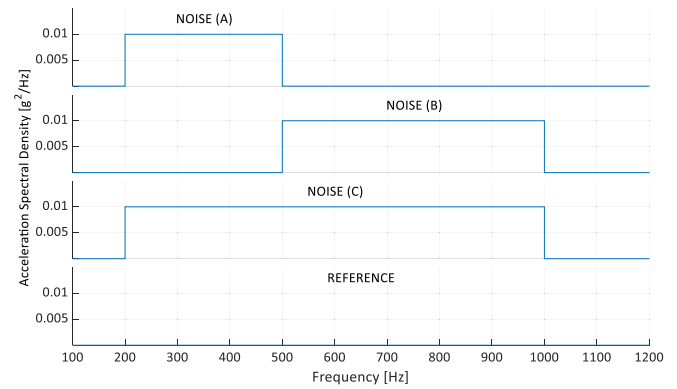


Fig. 1. Illustration of the four proposed operating conditions identified by different vibration noise levels, from Noise (A) at the top, then Noise (B), Noise (C), and the reference.

In particular, the device is a 22-kN shaker by Sentek Dynamics that can achieve a maximum peak displacement of $\pm 25 \text{ mm}$. The features of the selected shaker comply with the requirements imposed by the test plan in terms of peak acceleration (maximum acceleration of the shaker is 100 g in the case of light payloads) and frequency range (the admissible range varies from 2 Hz up to 2 kHz). The shaker requires an adequate calibrated controller, which acquires data from a calibrated 3056B2 piezoelectric accelerometers from Dytran Instruments. The controller generates a control feedback to precisely adjust the vibration produced by the shaker during the test based on the measurements acquired by the accelerometer. In the presented case, two accelerometers are used. One of them is installed on the external fixture used to mount the device on the shaker and is responsible for the control feedback. In this way, the device is guaranteed to endure the actual acceleration profiles. The other one is mounted on the body of the shaker, which could experience vibration levels different from the device, and it is used only for monitoring purposes.

The shaker included in the proposed experimental platform is a single-axis device that generates vibration toward a single direction. In order to test the performances of the device toward three different directions (x , y , and z), the fixture of the device to the table must be adjusted. In particular, the z -axis test can be performed using a standard shaker configuration (i.e., vibration is applied toward vertical direction), while a slip table must be used to repeat the experiments toward x - and y -axes (i.e., vibration is performed horizontally, and device fixture is rotated to ensure both x - and y -directions).

The random vibration noise described above is insufficient to ensure a complete analysis of the IMU's performance under dynamic conditions. It is also fundamental to develop a reproducible, controlled, and automated low-frequency movement that represents the vehicle's actual movement that the IMU must be able to detect and measure. In other words, this movement represents the actual input signal of the IMU, and the device needs to acquire this signal without distortion. Simultaneously, the device responses will be influenced by the random vibration in Fig. 1, which represents the measurement noise caused by the actual installation on the vehicle. It is essential that the low-frequency movement is acquired, maximizing the accuracy in order to ensure a reliable

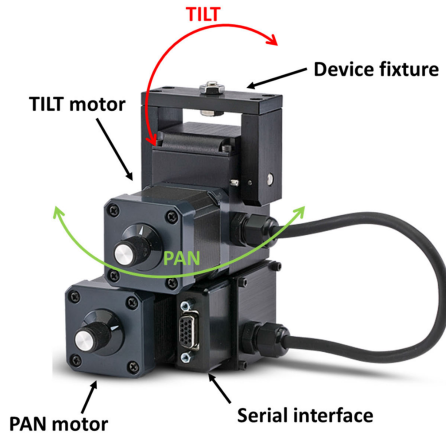


Fig. 2. Photograph of the PTU used to generate the controlled and reproducible movement. The red and green double arrows represent the direction of the TILT and PAN rotation, respectively.

position estimation by the suitable algorithms that are usually implemented. Ideally, the sensors should be able to acquire this movement in compliance with the metrological characteristics defined by the manufacturer.

A Pan Tilt Unit PTU-46-17.5 has been used to generate such basic low-frequency movements. This device precisely moves small objects, with a maximum payload of 1.81 kg. The PTU uses a serial communication interface to communicate with a control unit. The latter, in our case, is a simple laptop with a customized Python interface used for real-time movement control. The selected baud rate is the maximum available (34 800) to ensure fluidity and smoothness of the movements. Furthermore, the PTU allows controlling the speed, acceleration, and angular limit of the movement toward two different axes of rotation:

- 1) x -axis: not feasible.
- 2) y -axis: TILT rotation.
- 3) z -axis: PAN rotation.

For the sake of completeness of the analysis, the proposed analysis includes three different sets of movements, as follows:

- 1) P-movement (limited only to PAN movement, i.e., z -axis rotation).
- 2) T-movement (limited only to TILT movement, i.e., y -axis rotation).
- 3) C-movement (performed by combining the PAN and TILT movements, with a simultaneous rotation toward y - and z -axes).

A photograph of the PTU highlighting the direction of the PAN rotation (green arrow) and TILT rotation (red arrow) is shown in Fig. 2. The maximum angular aperture in each movement of the PTU is limited by some physical constraints related to the device's structure. The specific maximum aperture is provided as a function of the variable r_α which represents the angular position resolution.

More in detail, consider the following angular resolution:

$$r_\alpha = 0.051^\circ. \quad (1)$$

Then, the maximum aperture for the TILT movement $\text{TILT}_{\alpha_{\text{MAX}}}$ and the maximum aperture for the PAN movement

$\text{PAN}_{\alpha_{\text{MAX}}}$ are given by the following equations:

$$\begin{aligned} \text{TILT}_{\alpha_{\text{MAX}}} &= [-909 \cdot r_\alpha \div 604 \cdot r_\alpha] \\ &= [-46.356^\circ \div 30.804^\circ] \end{aligned} \quad (2)$$

$$\begin{aligned} \text{PAN}_{\alpha_{\text{MAX}}} &= [-3103 \cdot r_\alpha \div 3103 \cdot r_\alpha] \\ &= [-158.253^\circ \div 158.253^\circ]. \end{aligned} \quad (3)$$

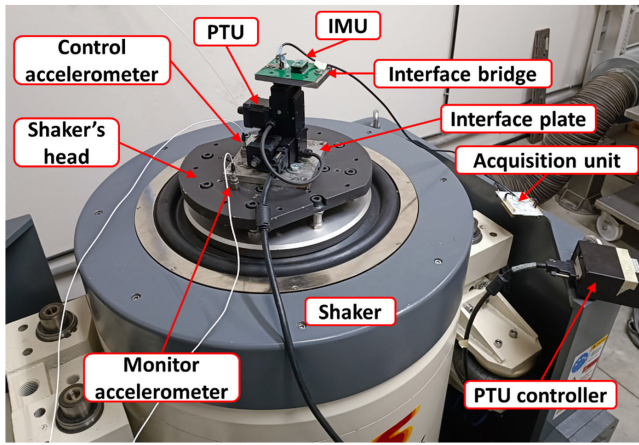
Thus, the following three sequences for the described sets of movements have been considered.

- 1) *P-Movement*: Start from position 0 (central step of the PTU), then moves toward $1750 \cdot r_\alpha$ before inverting the direction toward $-1750 \cdot r_\alpha$, and finally heading toward 0 after another direction inversion.
- 2) *T-Movement*: Start from position 0 (central step of the PTU), then moves toward $561 \cdot r_\alpha$ before inverting the direction toward $-800 \cdot r_\alpha$, and finally heading toward 0 after another direction inversion.
- 3) *C-Movement*: Combination of P-movement and T-movement carried out simultaneously.

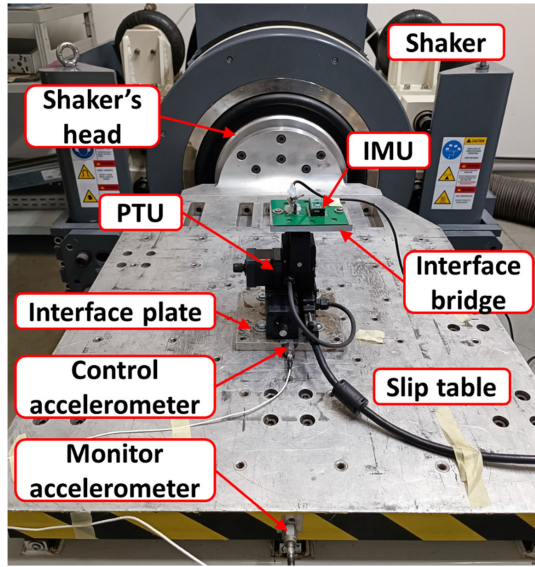
The P-movement is the widest set in terms of angle aperture, with a maximum coverage of 180° , while the T-movement covers only 70° due to physical constraints. For the sake of completeness of the investigation, each one of the previous movements has been repeated changing speed and acceleration. Three different sets of speed/acceleration (given as a function of the angular position resolution r_α) have been considered:

- 1) speed set V0
 - a) P-movement: speed of $1125 r_\alpha/\text{s}$ and acceleration equal to $2400 r_\alpha/\text{s}^2$.
 - b) T-movement: speed of $800 r_\alpha/\text{s}$ and acceleration equal to $2000 r_\alpha/\text{s}^2$.
 - c) C-movement: equal to P-movement for the PAN rotation; equal to C-movement for the TILT rotation.
- 2) speed set V1
 - a) P-movement: speed of $2250 r_\alpha/\text{s}$ and acceleration equal to $2400 r_\alpha/\text{s}^2$.
 - b) T-movement: speed of $1600 r_\alpha/\text{s}$ and acceleration equal to $2000 r_\alpha/\text{s}^2$.
 - c) C-movement: equal to P-movement for the PAN rotation; equal to C-movement for the TILT rotation.
- 3) speed set V2
 - a) P-movement: speed of $2250 r_\alpha/\text{s}$ and acceleration equal to $4800 r_\alpha/\text{s}^2$.
 - b) T-movement: speed of $1600 r_\alpha/\text{s}$ and acceleration equal to $4000 r_\alpha/\text{s}^2$.
 - c) C-movement: equal to P-movement for the PAN rotation; equal to C-movement for the TILT rotation.

The repetition of the same movement with different sets of speed and acceleration allows studying the influence of this parameter on the performances of the IMU. Since the goal is not to characterize or calibrate IMUs, the experimental setup has been designed to be simple and inexpensive, involving that tests along each axis under analysis were conducted by shifting



(a)



(b)

Fig. 3. Complete experimental setup for the dynamic characterization of IMU under vibration conditions: (a) implemented setup for vertical vibration noise (i.e., noise applied on the z -axis) and (b) implemented setup for horizontal vibration noise (i.e., noise applied on x -axis or y -axis).

the anchorage of the PTU relative to the direction of the IMU axis and the direction of shaker excitation. It is important to note that the speed and acceleration of the T-movement are slower than the values given for the P-movement. This is because the P-movement is wider than the T-movement, and thus, it requires more time to be completed. However, using the abovementioned speed sets, the P-movement and T-movement are characterized by the same time length, producing a fluid and smooth rotation when combined with the C-movement. After fixing a type of movement (i.e., P-movement, T-movement, or C-movement) and a speed set (i.e., V_0 , V_1 , or V_2), 30 consecutive repetitions of the same movement are implemented for the sake of measurement repeatability. Between two consecutive repetitions, the PTU remains still in the static neutral position for 5 s. A photograph of the complete experimental setup is illustrated in Fig. 3(a) in the case of vertical vibration noise (i.e., noise applied toward the z -axis) and in Fig. 3(b) in the case of horizontal vibration noise (i.e., noise applied toward the x -axis, while noise applied toward the y -axis is obtained simply rotating the PTU of 90°).

TABLE I
TRANSMISSIBILITY VALUES OF THE PROPOSED EXPERIMENTAL SETUP IN THREE DIFFERENT FREQUENCY RANGES

Frequency range	Transmissibility	
	Mean value	Standard Deviation
$[20 \div 200]$	0.99971	0.00015
$[200 \div 500]$	1.00855	0.00021
$[500 \div 1000]$	1.01251	0.00025

Along with the IMU under test and the PTU, the complete experimental setup includes the following.

- 1) A vibration-producing device (i.e., the shaker).
- 2) An aluminum interface plate called a fixture which is used to connect the shaker's head with the PTU (in the case of vertical vibration) or the shaker's slip table with the PTU (in the case of horizontal vibration). The interface plate has been fixed to the shaker's head or the slip table using four M8 screws, while the clamping between the fixture and the PTU has been achieved with four M6 screws on the bottom of the PTU.
- 3) An interface plate bridge made of aluminum is used to connect the PTU and the device under test. Also, in this case, clamping has been achieved with adequate screws.
- 4) A control accelerometer is located on the fixture and used to ensure that the required vibration from the test plan is correctly applied on the device.
- 5) A monitor accelerometer is used to check whether the shaker is producing the correct vibration or not.

The vibration shaker is used to provide high-frequency random vibration noise to emulate the real operating conditions in terrestrial vehicles. The PTU is mounted on top of the shaker and is used to generate the low-frequency movement that the IMU should detect and measure. Furthermore, an acquisition unit composed of a Nucleo-64 board and a laptop is used to acquire and store the data from the IMU.

In order to validate the applicability of the proposed setup, the transmissibility has been determined. This value represents the ratio between the vibration measured by the two accelerometers, one of them located on the shaker and the other one on the fixture. The mean value and the standard deviation calculated on three frequency ranges are reported in Table I. The closest the transmissibility is to 1, the better the fixture validation in terms of stiffness and transmission capabilities.

III. DEVICE UNDER TEST

The device considered in this work is a low-cost commercial IMU widely used for several applications. The metrological (sensitivity, full scale, and zero-level) and functional (temperature and voltage range, data output, interfaces, etc.) characteristics of the device are reported in Table II according to the manufacturer's datasheet [33]. The maximum output data rate (ODR) available for all the embedded sensors in the IMU is 119 Hz, which automatically introduces an antialiasing low-pass filter (LPF) with a 50-Hz cutoff frequency. Considering the selected ODR, the IMU has different theoretical responses when subjected to the excitation described

TABLE II

EXTRACT OF THE DATASHEET OF THE CONSIDERED IMU, INCLUDING THE MAJOR METROLOGICAL CHARACTERISTICS

SENSOR	PARAMETER	VALUE
Complete IMU	Temperature range	$-40\text{ }^{\circ}\text{C} \div 85\text{ }^{\circ}\text{C}$
	Power supply	$1.9\text{ V} \div 3.6\text{ V}$
	Data output	16 bit
	Interfaces	SPI / I ² C
	Package technology	LGA
	Manufacturing	MEMS
	Output Data Rate	119 Hz
	Anti-Aliasing filter	50 Hz
Accelerometer	Axes	3
	Full scale	$\pm 2\text{ g} / \pm 4\text{ g} / \pm 8\text{ g} / \pm 16\text{ g}$
	Typical zero-g level offset accuracy	$\pm 90\text{ mg}$ @ $\pm 8\text{ g}$ full scale
	Sensitivity	0.732 mg/LSB @ $\pm 16\text{ g}$ full scale
Gyroscope	Axes	3
	Full scale	$\pm 245\text{ dps} / \pm 500\text{ dps} / \pm 2000\text{ dps}$
	Typical zero-rate level	$\pm 30\text{ dps}$ @ $\pm 2000\text{ dps}$ full scale
	Sensitivity	70 mdps/LSB @ $\pm 2000\text{ dps}$ full scale
Magnetometer	Axes	3
	Full scale	$\pm 4\text{ gauss} / \pm 8\text{ gauss} / \pm 12\text{ gauss} / \pm 16\text{ gauss}$
	Typical zero-gauss level	$\pm 1\text{ gauss}$ @ $\pm 4\text{ gauss}$ full scale
	Sensitivity	0.58 mgauss/LSB @ $\pm 16\text{ gauss}$ full scale
Temperature transducer	Sensitivity	$16\text{ LSB}/^{\circ}\text{C}$
	Typical 0-level output	$25\text{ }^{\circ}\text{C}$

in Section II. A summary of such performances is reported in Table III.

Most of the errors and influencing factors come out from the mechanical assembly of the test bench. Analyzing the contributions one by one, we can group them into the errors introduced by positioning and the contribution due to the nonideal PTU. The former was handled by verifying the correct alignment of the parts on the shaker with a mechanical jig, while the latter, due to its mechanical characteristics, can be neglected.

IV. TIME-DOMAIN ANALYSIS

In this section, the response of the IMU during the test plan illustrated in Section II is reported considering a time-domain analysis to emphasize how the actual conditions typical of the automotive field influence the ideal response of the accelerometer and gyroscope sensors.

In this point of view, specific metrics will be introduced.

For a first qualitative analysis, the output of the triaxial gyroscope embedded in the IMU under test is illustrated using

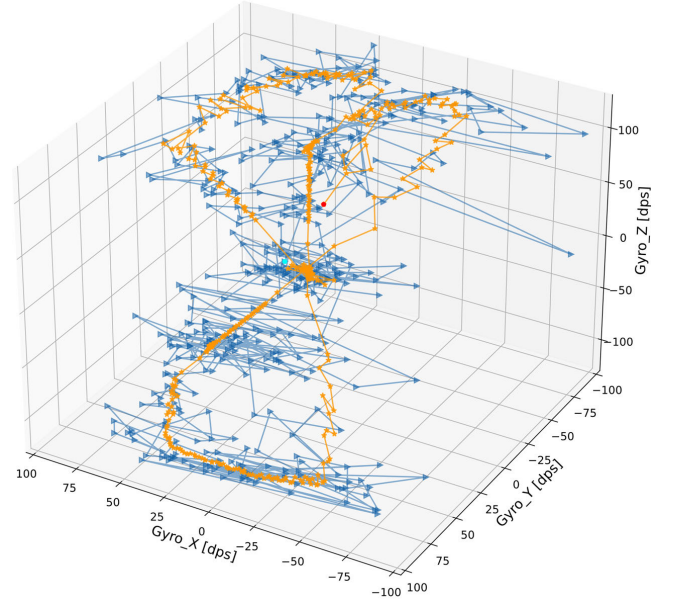


Fig. 4. 3-D acquisition of the gyroscope toward x-, y-, and z-axes during the proposed test plan in the presence of Noise A (blue trend) and standard conditions (orange trend).

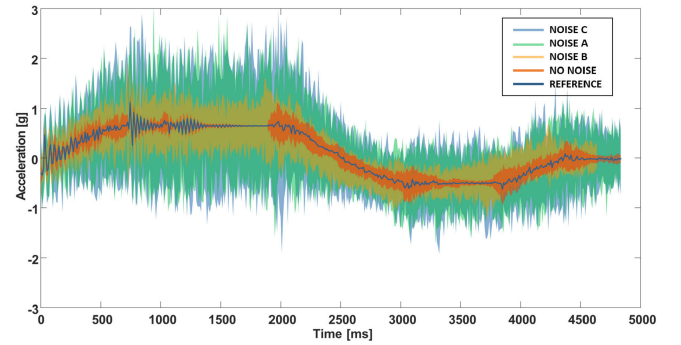


Fig. 5. Data dispersion for the x-axis of the accelerometer under different operating conditions (random vibration noise applied toward the y-axis).

a 3-D plot in Fig. 4. Two different cases are taken into account: a reference condition in which no additional noise is applied, and Noise (A) operating condition where a random vibration noise in the 200 Hz \div 500-Hz bandwidth is applied.

The data in Fig. 4 refer only to a single repetition (R10) of the C-movement with a V2 speed set and vibration noise applied toward the x-axis. However, it is clearly analyzing Fig. 4 that the vibration noise introduced by the shaker is not entirely rejected by the IMU, and thus, its response is partially influenced by the operating conditions. More specifically, such influence is reflected in a data dispersion phenomenon for every axis of every sensor. For instance, two examples of the data dispersion are illustrated in Figs. 5 and 6, considering the C-movement with the V1 speed set. More in detail, Fig. 5 refers to the x-axis of the accelerometer while noise is applied on the y-axis. Similarly, Fig. 6 illustrates the x-axis of the gyroscope while noise is applied on the y-axis.

Both Figs. 5 and 6 illustrate the noise as a color bandwidth centered in the average value in standard conditions (continuous blue line) and characterized by an amplitude equal to two

TABLE III
THEORETICAL RESPONSE OF THE IMU WITH RESPECT TO THE TWO EXTERNAL STIMULI INCLUDED IN THE PROPOSED TEST PLAN

STIMULUS	DEVICE	AIM	FREQUENCY RANGE	IDEAL RESPONSE
Random Vibration	Shaker	Wideband noise used to emulate the actual operating conditions in automotive field of application.	Different spectral components between 200 Hz and 1 kHz	It should be completely rejected by the IMU, and it should not be visible on the device's response since the lowest component of the noise is at least 4 times higher than the cut-off frequency of the LPF.
Controlled movement	PTU	Actual signal to be acquired based on a 3-dimensional movement at different speed, acceleration and direction	Very low frequency movement below few Hz.	It should be properly measured and registered by the considered IMU without distortion since it is fully enclosed in the LPF bandwidth.

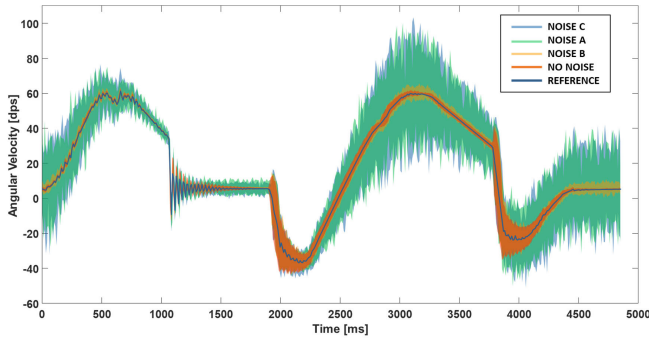


Fig. 6. Data dispersion for the x -axis of the gyroscope under different operating conditions (random vibration noise applied toward the y -axis).

times the standard deviation. Analyzing both Figs. 5 and 6 clearly emerge a nonnegligible impact of the vibration noise typical of the automotive field with respect to the standard operating conditions.

Figs. 5 and 6 emphasize that some dispersion characterizes both the accelerometer and gyroscope, even in standard operating conditions. This dispersion slightly increases in the presence of Noise B (limited to $500 \text{ Hz} \div 1000 \text{ Hz}$), while it remarkably raises when either Noise A (limited to $200 \text{ Hz} \div 500 \text{ Hz}$) or Noise C (complete bandwidth between 200 and 1000 Hz) is considered. This could be verified for almost every test repetition, regardless of the considered sensor's axis, in the case of both accelerometer and gyroscope. However, it is essential to introduce an adequate metric to quantify this phenomenon and consider the nonideality of the internal antialiasing LPF. To fill this gap, the data dispersion \overline{DD}_k on the k -axis has been defined as the average value (which is calculated on the entire length of a single movement) of the standard deviation on every sample for every repetition as

$$\overline{DD}_k = \frac{1}{m} \sum_{j=1}^m \left(\sqrt{\frac{1}{n-1} \sum_{i=1}^n (s_{i,j,k} - \mu_{s,j,k})^2} \right) \quad (4)$$

where

- 1) m = number of samples in a single movement;
- 2) $n = 30$ = number of repetitions of the same movement;
- 3) $s_{i,j,k}$ = j th value acquired by a specific sensor toward the k -axis during the i th repetition.
- 4) $\mu_{s,j,k}$ = average value of the j th sample acquired by a specific sensor toward the k -axis on all the repetitions.

The data dispersion calculated for both accelerometer and gyroscope is reported in Tables IV and V, respectively, considering all four operative conditions applied toward x -, y -, and z -directions, all three movements, all three speed sets, and all the axis. Despite the presence of the 50-Hz antialiasing filter, it can be observed from Tables III and IV that the application of the high-frequency vibration noise increases the dispersion of the data, regardless of the axis of excitation and the noise bandwidth.

The only exception has been found in the gyroscope y -axis, where NOISE B applied along the z - or y -direction does not significantly influence the normal dispersion of the sensor in standard conditions. This indicates a better rejection of the frequency noise for the gyroscope, especially on the y -axis. However, when lower spectral components of the noise are applied (i.e., Noise A and Noise C), the gyroscope suffers from significant dispersion. Overall, the NOISE B band is the one that causes the most negligible increase in dispersion in all the considered sensors and operating scenarios.

Instead, the maximum values of the dispersion \overline{DD}_k have been found in the case of NOISE A and NOISE C, as shown in Table VI, where the maximum dispersion values for each sensor axis are compared considering the presence or absence of the random vibration noise.

A summary of the data dispersion is reported in Figs. 7 and 8 for the accelerometer and gyroscope, respectively. Each group of bars represents the same operating conditions, where the height of the bars stands for the average value of the \overline{DD}_k between different speed sets and different movements, while the black vertical line represents the standard deviation.

The blue bars in Figs. 7 and 8 stand for the application of the noise toward the z -axis, while the orange and green bars stand for the y - and x -directions of application of the noise, respectively. Finally, each subplot refers to a different axis of acquisition of the sensor. From Figs. 7 and 8, some considerations can be drawn.

- 1) The y -axis of acquisition of the accelerometer is the most affected by the dispersion regardless of the noise level, while the x -axis presents a good rejection.
- 2) The accelerometer shows the worst behavior when the noise is applied along the x -direction, while it performs better in the case of noise applied along z .

TABLE IV
SUMMARY OF THE DATA DISPERSION EVALUATED FOR THE ACCELEROMETER FOR EVERY OPERATING CONDITION
AND EVERY MOVEMENT. LINEAR ACCELERATION [G]

SENSOR	NOISE DIRECTION	OPERATING CONDITION	LINEAR ACCELERATION [g]								
			P-MOVEMENT			T-MOVEMENT			C-MOVEMENT		
			V0	V1	V2	V0	V1	V2	V0	V1	V2
Accelerometer X-axis	X	Reference	0.081	0.080	0.088	0.172	0.226	0.258	0.141	0.156	0.182
		NOISE A	1.160	1.176	1.241	1.337	1.354	1.354	0.989	0.943	1.010
		NOISE B	1.156	1.109	1.083	1.506	1.530	1.536	1.129	0.990	0.880
		NOISE C	1.643	1.746	1.707	1.844	1.910	1.839	1.387	1.290	1.284
	Y	Reference	0.120	0.097	0.121	0.127	0.195	0.197	0.125	0.152	0.161
		NOISE A	0.736	0.769	0.739	0.632	0.667	0.641	0.792	0.862	0.872
		NOISE B	0.373	0.390	0.359	0.245	0.305	0.311	0.374	0.428	0.440
		NOISE C	0.839	0.851	0.865	0.674	0.750	0.711	0.834	0.972	0.980
	Z	Reference	0.105	0.117	0.127	0.134	0.227	0.225	0.123	0.160	0.160
		NOISE A	0.322	0.326	0.331	0.444	0.486	0.503	0.310	0.337	0.337
		NOISE B	0.216	0.220	0.230	0.267	0.317	0.319	0.229	0.266	0.273
		NOISE C	0.377	0.378	0.382	0.514	0.571	0.581	0.371	0.404	0.421
Accelerometer Y-axis	X	Reference	0.114	0.084	0.082	0.349	0.316	0.301	0.267	0.238	0.234
		NOISE A	10.363	10.673	11.333	4.096	4.138	4.081	9.097	9.078	9.186
		NOISE B	5.006	4.740	4.589	2.345	2.335	2.348	4.720	4.573	3.945
		NOISE C	10.648	10.838	11.007	4.341	4.474	4.335	9.359	8.920	9.025
	Y	Reference	0.110	0.089	0.092	0.190	0.243	0.237	0.183	0.218	0.211
		NOISE A	4.847	4.874	4.779	6.314	6.225	6.228	5.176	4.166	4.329
		NOISE B	1.087	1.103	1.032	1.460	1.518	1.492	1.272	1.113	1.085
		NOISE C	5.173	5.086	5.164	6.980	6.875	6.925	5.317	4.363	4.648
	Z	Reference	0.082	0.074	0.081	0.180	0.264	0.288	0.160	0.206	0.194
		NOISE A	1.647	1.571	1.574	1.286	1.362	1.382	1.626	1.584	1.677
		NOISE B	0.368	0.363	0.360	0.391	0.416	0.407	0.361	0.354	0.346
		NOISE C	2.165	2.131	2.143	1.541	1.530	1.589	1.817	1.791	1.823
Accelerometer Z-axis	X	Reference	0.054	0.046	0.043	0.169	0.160	0.192	0.114	0.094	0.101
		NOISE A	2.836	2.895	3.112	3.218	3.129	3.133	2.417	2.340	2.449
		NOISE B	2.298	2.234	2.157	2.520	2.440	2.444	2.218	2.026	2.205
		NOISE C	3.470	3.624	3.584	3.794	3.716	3.644	3.067	2.862	2.893
	Y	Reference	0.045	0.041	0.042	0.102	0.125	0.136	0.086	0.093	0.089
		NOISE A	1.795	1.862	1.778	1.196	1.205	1.196	1.756	1.733	1.794
		NOISE B	0.616	0.613	0.570	0.459	0.503	0.504	0.628	0.610	0.604
		NOISE C	1.999	1.985	1.998	1.316	1.340	1.369	1.774	1.824	1.896
	Z	Reference	0.059	0.060	0.063	0.091	0.138	0.141	0.084	0.096	0.088
		NOISE A	0.676	0.680	0.681	0.758	0.772	0.780	0.644	0.624	0.627
		NOISE B	0.296	0.298	0.307	0.374	0.381	0.402	0.322	0.305	0.307
		NOISE C	0.745	0.746	0.749	0.807	0.823	0.842	0.695	0.681	0.700

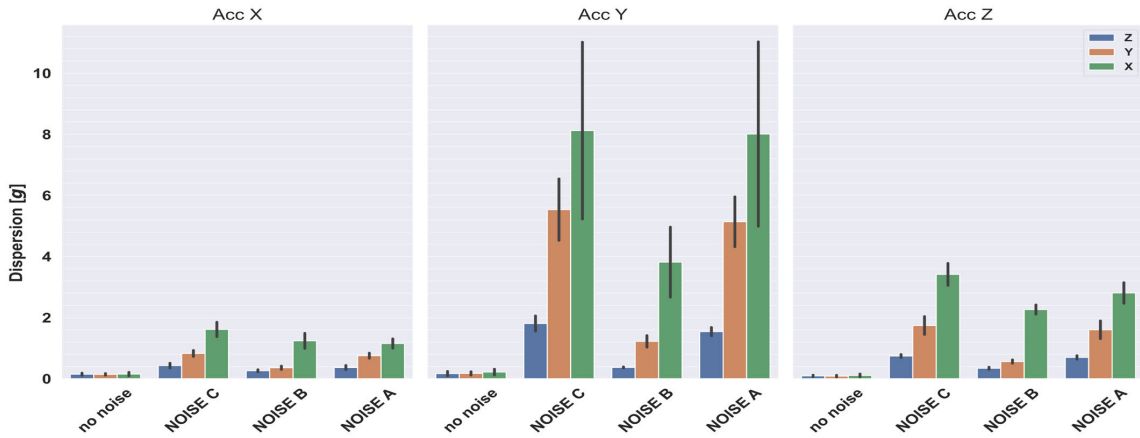


Fig. 7. Mean and standard deviation of the data dispersion for the accelerometer considering different bandwidths and different axes of application of the noise.

- 3) The gyroscope has better rejection performances (i.e., lower dispersion) when noise is applied along the z-direction, while the performances in the case of x- and y-directions of applications of the noise are comparable.
- 4) Opposite to the accelerometer, the x-axis of the gyroscope is characterized by the highest dispersion.

V. FREQUENCY-DOMAIN ANALYSIS

Due to the presence of the 50-Hz antialiasing filter, all the spectral components of the random vibration noise generated in different operating conditions should not be visible in the frequency response of the IMU. Instead, the vibration noise is present in the IMU's response as an aliasing issue that

TABLE V
SUMMARY OF THE DATA DISPERSION EVALUATED FOR THE GYROSCOPE FOR EVERY OPERATING CONDITION AND EVERY MOVEMENT

SENSOR	NOISE DIRECTION	OPERATING CONDITION	ANGULAR RATE [dps]								
			P-MOVEMENT			T-MOVEMENT			C-MOVEMENT		
			V0	V1	V2	V0	V1	V2	V0	V1	V2
Gyroscope X-axis	X	Reference	0.492	0.628	0.663	1.281	1.531	1.471	1.281	2.514	2.646
		NOISE A	24.409	25.173	27.215	12.440	12.463	12.353	21.764	22.153	22.741
		NOISE B	8.056	7.766	7.580	3.777	4.013	4.090	8.066	8.340	6.875
		NOISE C	25.597	28.067	29.167	11.934	12.335	12.029	20.386	20.206	20.373
	Y	Reference	0.523	0.623	0.655	0.926	1.236	1.271	1.179	3.393	3.895
		NOISE A	17.808	17.833	17.525	23.790	23.506	23.101	19.629	16.573	17.223
		NOISE B	1.785	1.925	1.789	2.542	2.950	2.924	2.545	4.074	4.186
		NOISE C	18.731	18.405	18.716	25.507	24.984	24.846	19.750	17.088	18.041
	Z	Reference	0.449	0.596	0.600	0.785	1.328	1.522	0.901	2.955	3.596
		NOISE A	6.586	6.362	6.411	4.764	5.046	5.113	6.570	7.128	7.746
		NOISE B	0.814	0.844	0.851	1.078	1.220	1.264	1.208	2.072	2.919
		NOISE C	7.678	7.514	7.590	5.822	5.778	5.916	6.943	7.524	7.958
Gyroscope Y-axis	X	Reference	0.359	0.587	0.575	2.930	4.718	5.805	2.030	3.409	3.814
		NOISE A	5.513	5.156	5.368	7.548	9.260	9.009	5.334	7.178	7.371
		NOISE B	1.791	1.770	1.751	3.907	5.610	5.560	3.649	4.676	5.398
		NOISE C	6.210	6.657	6.344	7.379	8.832	9.050	5.689	7.702	7.323
	Y	Reference	0.361	0.588	0.614	2.668	4.342	4.884	1.584	3.840	4.405
		NOISE A	6.010	6.601	6.231	5.181	7.058	6.974	7.138	9.520	9.885
		NOISE B	0.638	0.837	0.803	2.107	4.857	5.541	1.702	3.957	4.083
		NOISE C	6.310	6.603	6.590	5.155	7.262	7.341	6.958	9.568	9.831
	Z	Reference	0.395	0.594	0.581	2.298	4.822	5.593	1.453	3.594	4.408
		NOISE A	2.296	2.409	2.439	4.458	6.557	7.211	2.598	4.466	5.245
		NOISE B	0.445	0.577	0.562	1.933	4.242	4.050	1.400	2.522	3.654
		NOISE C	2.272	2.439	2.378	4.349	6.731	6.899	3.042	4.962	6.003
Gyroscope Z-axis	X	Reference	1.063	2.685	2.813	0.794	1.079	1.422	0.941	2.637	2.752
		NOISE A	8.412	9.982	10.468	8.409	8.234	7.976	7.630	9.856	9.462
		NOISE B	3.453	4.262	5.093	2.718	3.031	2.917	2.756	4.325	5.601
		NOISE C	8.947	10.994	11.176	8.566	8.680	8.724	8.033	9.978	9.446
	Y	Reference	1.441	4.580	4.951	0.772	1.012	1.181	1.032	4.302	4.665
		NOISE A	9.512	10.571	11.011	12.598	13.375	13.259	7.728	8.486	8.741
		NOISE B	1.837	3.865	4.420	0.955	1.391	1.486	1.375	4.115	4.020
		NOISE C	9.027	9.925	10.684	12.236	13.463	13.181	7.007	8.150	8.569
	Z	Reference	0.904	3.439	3.658	0.712	1.071	1.157	0.802	3.859	4.610
		NOISE A	3.217	5.711	4.971	2.574	2.822	2.863	3.445	5.538	6.433
		NOISE B	0.934	3.241	3.450	0.764	1.029	1.062	0.904	2.267	3.447
		NOISE C	3.184	5.469	4.943	2.963	3.323	3.445	3.292	5.378	6.489

TABLE VI

MAXIMUM DISPERSION OF ACCELEROMETER AND GYROSCOPE: COMPARISON BETWEEN REFERENCE AND ACTUAL OPERATING CONDITIONS

SENSOR	AXIS OF ACQ	MAX REFERENCE DISPERSION				MAX DISPERSION UNDER VIBRATION					$\Delta\%$
		VALUE	MOVEMENT	NOISE DIRECTION	SPEED SET	VALUE	MOVEMENT	NOISE DIRECTION	NOISE TYPE	SPEED SET	
Accelerometer	X	0.258 g	TILT	X	V2	1.910 g	TILT	X	Noise C	V1	+640%
	Y	0.349 g	TILT	X	V0	11.333 g	PAN	X	Noise A	V2	+3147%
	Z	0.192 g	TILT	X	V2	3.794 g	TILT	X	Noise C	V0	+1876%
Gyroscope	X	3.89 dps	COMBO	Y	V2	27.21 dps	PAN	X	Noise C	V2	+599%
	Y	5.80 dps	TILT	X	V2	9.88 dps	COMBO	Y	Noise A	V2	+70%
	Z	4.95 dps	PAN	Y	V2	13.46 dps	TILT	Y	Noise C	V1	+172%

changes the in-band behavior of the device. Figs. 9 and 10 show the power spectrum of the acquired data considering the x -axis of the accelerometer and the z -axis of the gyroscope, respectively. Both Figs. 9 and 10 refer to the C-movement with V0 speed set and vibration noise applied in different directions according to the various subplots. Analyzing the power spectrum, some considerations can be drawn.

- 1) The low-frequency peak represents the actual movement provided by the PTU and correctly sampled by the IMU.
- 2) Concerning the reference conditions, applying the vibration noise leads to an increase of the floor level in the frequency range of 5 Hz \div 50 Hz.
- 3) As a confirmation of the time-domain analysis, Noise (B) slightly increases the floor level of the gyroscope while it has a higher impact on the accelerometer.

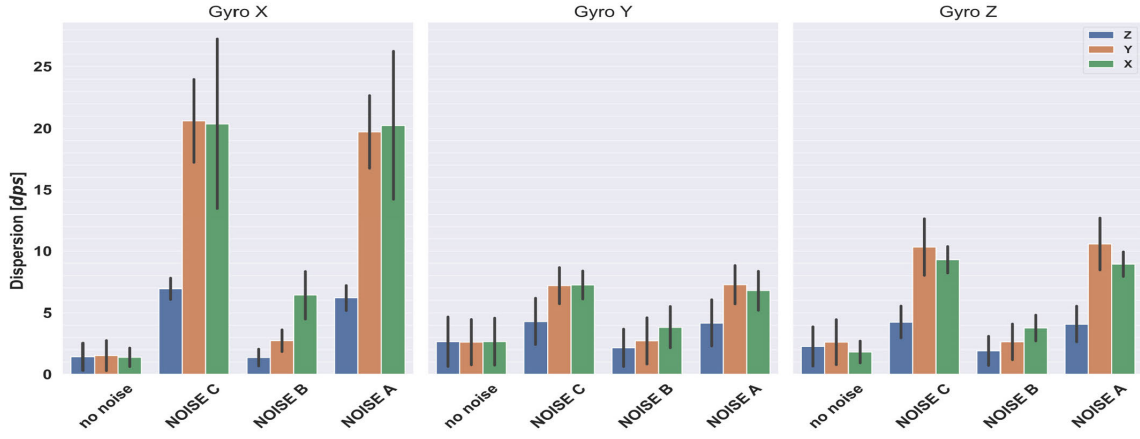


Fig. 8. Mean and standard deviation of the data dispersion for the gyroscope considering different bandwidths and different axes of application of the noise.

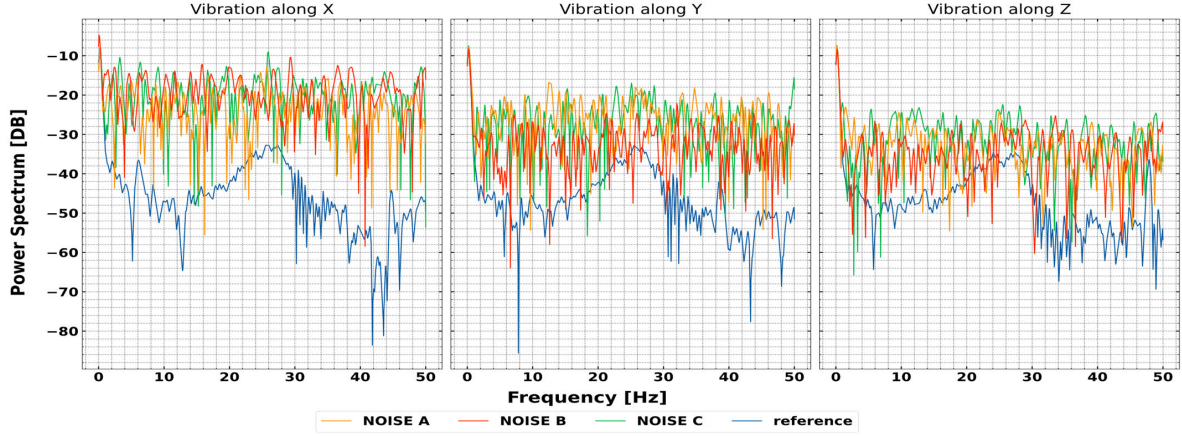


Fig. 9. Power spectrum for the x -axis of the accelerometer considering different bandwidths and different axes of application of the noise.

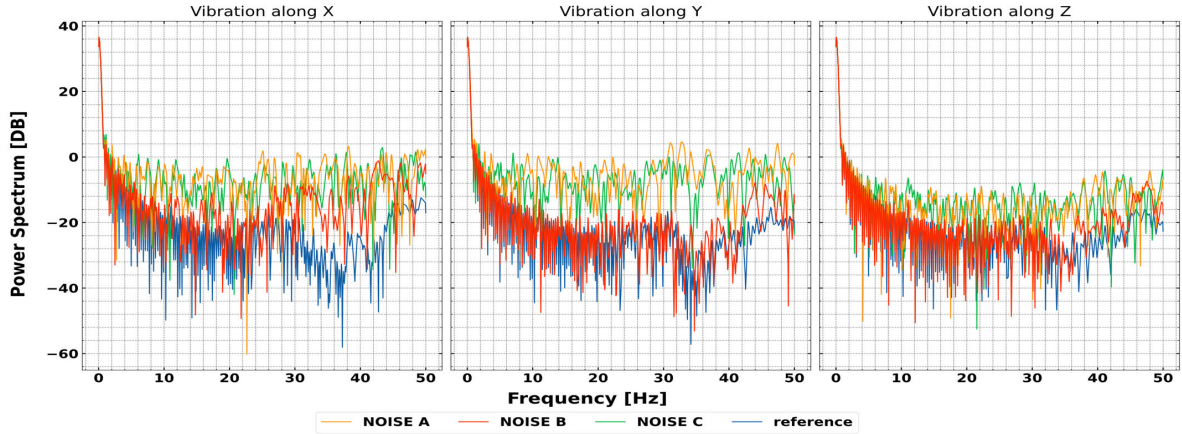


Fig. 10. Power spectrum for the z -axis of the gyroscope considering different bandwidths and different axes of application of the noise.

- 4) In all cases, Noise (C) and Noise (A) represent the worst operating conditions, with a significant impact on the IMU's power spectrum concerning standard operating conditions.

In order to quantify this impact, the delta floor ΔF_k , for the k th axis, has been introduced as the difference between the floor level of the power spectrum in the actual operating condition and the floor level of the reference condition F_{ref_k}

$$F_{\text{ref}_k} = \frac{1}{n} \sum_i^n 10 \log_{10}(\text{PS}(\text{ref}_i)) \quad (5)$$

$$\Delta F_k = \frac{1}{30} \sum_j^{30} \left(\frac{1}{n} \sum_i^n 10 \log_{10}(\text{PS}(s_{i,j_k})) - F_{\text{ref}_k} \right) \quad (6)$$

where n is the number of samples for a specific movement, ref is the reference operating conditions, and PS is the power spectrum evaluated using the Kaiser window, 100-Hz sampling frequency, and single-side fast Fourier transform (FFT) with a length of 8192. All the delta floor values evaluated for the accelerometer and gyroscope are reported in Tables VII and VIII, respectively, including every movement, every speed set, every noise level (in terms of bandwidth

TABLE VII

SUMMARY OF THE DELTA FLOOR PARAMETER EVALUATED FOR THE ACCELEROMETER FOR EVERY OPERATING CONDITION AND EVERY MOVEMENT

SENSOR	NOISE DIRECTION	OPERATING CONDITION	DELTA FLOOR [dB]								
			P-MOVEMENT			T-MOVEMENT			C-MOVEMENT		
			V0	V1	V2	V0	V1	V2	V0	V1	V2
Accelerometer X-axis	X	NOISE A	44.154	39.176	41.076	30.718	28.780	24.533	22.415	27.293	24.477
		NOISE B	48.467	41.134	43.658	32.656	30.240	25.996	26.513	28.398	24.600
		NOISE C	47.732	41.938	44.050	33.197	31.397	26.627	26.251	28.832	26.058
	Y	NOISE A	38.040	31.493	35.208	25.776	21.936	21.675	19.274	27.606	26.270
		NOISE B	32.029	24.779	28.525	17.354	14.561	14.465	13.749	21.935	20.736
		NOISE C	39.490	32.573	37.046	26.963	23.230	22.551	20.048	29.199	27.755
	Z	NOISE A	32.500	24.668	29.143	22.752	20.870	20.480	13.321	19.549	20.466
		NOISE B	28.037	20.557	24.933	17.648	16.749	16.648	12.317	18.298	19.236
		NOISE C	34.179	26.263	30.680	24.594	22.609	22.453	15.196	21.965	23.193
Accelerometer Y-axis	X	NOISE A	55.444	58.805	58.676	40.091	37.572	35.306	48.210	43.016	42.373
		NOISE B	50.054	51.173	50.824	34.178	30.765	29.270	43.584	35.787	34.572
		NOISE C	55.143	58.778	59.248	40.241	37.786	35.468	47.875	40.995	41.247
	Y	NOISE A	50.115	52.576	52.768	45.760	37.785	40.369	45.393	39.695	39.570
		NOISE B	37.714	40.162	40.033	33.295	26.159	28.391	33.065	27.516	26.080
		NOISE C	51.391	53.979	54.870	47.264	39.033	41.832	46.290	40.440	40.541
	Z	NOISE A	39.953	41.200	41.382	33.925	21.898	22.690	34.640	31.468	32.454
		NOISE B	27.671	28.661	28.512	23.348	13.591	13.036	21.103	17.681	17.984
		NOISE C	42.079	43.125	43.373	35.273	23.287	23.808	34.565	31.590	32.283
Accelerometer Z-axis	X	NOISE A	53.373	54.185	54.027	42.152	40.298	36.492	38.398	39.948	36.644
		NOISE B	54.976	53.455	53.322	40.364	37.850	34.696	40.222	39.798	36.331
		NOISE C	56.378	56.315	56.395	44.200	42.190	38.538	41.669	41.429	38.101
	Y	NOISE A	48.353	51.236	51.390	40.404	31.549	34.328	37.473	38.625	37.559
		NOISE B	38.888	40.823	40.765	29.726	22.428	24.777	29.108	27.181	26.109
		NOISE C	48.129	50.585	51.213	39.974	31.529	34.748	37.025	38.440	37.387
	Z	NOISE A	40.086	38.473	40.851	36.352	28.084	28.574	30.307	25.107	26.892
		NOISE B	32.885	31.186	34.209	29.071	20.993	22.204	26.220	20.227	21.999
		NOISE C	40.452	39.081	41.067	36.554	28.315	29.212	30.651	25.873	27.519

TABLE VIII

SUMMARY OF THE DELTA FLOOR PARAMETER EVALUATED FOR THE GYROSCOPE FOR EVERY OPERATING CONDITION AND EVERY MOVEMENT

SENSOR	NOISE DIRECTION	OPERATING CONDITION	DELTA FLOOR [dB]								
			P-MOVEMENT			T-MOVEMENT			C-MOVEMENT		
			V0	V1	V2	V0	V1	V2	V0	V1	V2
Accelerometer X-axis	X	NOISE A	46.539	48.016	44.615	30.766	28.809	25.597	28.279	24.797	22.289
		NOISE B	38.518	38.353	34.720	20.191	19.331	16.472	21.138	16.538	12.852
		NOISE C	45.571	48.218	46.349	30.147	28.566	25.199	26.834	22.126	20.370
	Y	NOISE A	44.532	45.994	46.322	38.652	32.307	34.002	31.820	27.096	26.055
		NOISE B	24.394	26.207	25.240	19.157	15.388	16.785	13.008	14.947	13.248
		NOISE C	45.021	46.378	47.060	39.244	32.817	34.634	31.986	27.267	26.275
	Z	NOISE A	33.206	34.524	35.618	23.816	18.169	18.421	20.572	20.803	20.028
		NOISE B	15.555	16.494	17.098	10.859	8.114	8.618	5.824	14.214	13.170
		NOISE C	35.507	36.799	38.284	26.110	19.858	20.133	21.142	21.481	20.666
Accelerometer Y-axis	X	NOISE A	38.588	35.735	35.524	13.774	12.511	9.618	7.129	14.025	10.983
		NOISE B	30.781	26.816	25.967	7.742	5.673	5.606	5.883	11.729	9.048
		NOISE C	37.340	35.930	35.369	13.144	11.685	9.049	7.228	13.328	10.341
	Y	NOISE A	32.582	33.912	33.553	11.498	10.194	9.533	7.260	19.672	18.511
		NOISE B	14.860	16.259	16.148	4.059	5.839	5.633	2.586	14.211	12.977
		NOISE C	32.172	33.046	32.802	10.909	9.999	9.429	6.741	19.394	17.878
	Z	NOISE A	28.185	28.712	28.623	9.531	13.642	12.916	5.012	15.586	13.899
		NOISE B	11.529	13.674	13.175	3.660	10.102	8.796	2.818	13.643	11.813
		NOISE C	27.615	28.933	28.509	9.610	13.583	12.841	4.706	15.693	13.815
Accelerometer Z-axis	X	NOISE A	18.380	17.083	16.580	30.206	27.422	21.679	15.844	16.732	12.486
		NOISE B	11.471	10.200	9.013	18.062	17.035	11.931	8.390	10.984	8.519
		NOISE C	18.006	16.970	17.179	30.276	27.451	22.489	15.108	15.405	11.527
	Y	NOISE A	21.273	22.603	24.218	37.142	34.957	34.926	17.597	18.604	18.396
		NOISE B	4.383	10.156	9.912	11.850	12.015	12.188	3.549	13.243	12.485
		NOISE C	20.869	22.113	23.775	36.490	34.777	34.712	16.573	17.872	17.547
	Z	NOISE A	9.314	14.275	12.924	21.500	22.246	19.945	8.401	15.985	14.807
		NOISE B	2.624	11.737	8.879	7.596	11.716	9.351	1.993	12.759	12.111
		NOISE C	9.998	14.747	13.553	23.395	25.357	22.023	8.659	15.534	14.845

and direction of application), and every axis of the sensors. Looking at both Tables VII and VIII, some considerations can be drawn.

- 1) There is not a particular correlation between different speed sets and the changes in the ΔF_k for both sensors and all three axes. For instance, the x -axis of the

gyroscope and the y -axis of the accelerometer suffer, particularly the speed set V_0 , with a higher increase of the ΔF_k . Quite the opposite, looking at the x -axis of the accelerometer and z -axis of the gyroscope, the same V_0 speed set produces the lowest increase of the delta floor.

- 2) As a confirmation of the results obtained in the time-domain analysis, Noise (C) leads to the highest increase of ΔF_k , followed by Noise (A) and then Noise (B).
- 3) The gyroscope's response emphasizes better performance with respect to the accelerometer, especially in rejecting Noise (B).

VI. CONCLUSION

This work illustrates an experimental characterization of the IMU under dynamic operating conditions typical of the automotive field. A specific platform and a customized test plan have been developed to simultaneously excite the IMU with a low-frequency stimulus provided by a PTU (the actual movement that the IMU must properly acquire) and a high-frequency vibration noise (that should be wholly rejected) provided by a shaker. Two analyses have been carried out to quantitatively estimate the impact of the noisy conditions on the IMU's response.

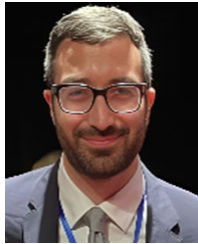
A time-domain analysis has been useful for introducing a data dispersion parameter, while the frequency-domain analysis allowed evaluating the increase in the delta floor level caused by the additional noise. This study carried out interesting results inherent to the unexpected behavior of low-cost IMUs operating under dynamic conditions while applying a different vibration stress typical of the actual operating conditions in the automotive field of applications. More in detail, vibration influences the correct operation of such devices, which could reasonably worsen their usage in various applications such as positioning algorithms.

Future developments will regard the metrological verification and calibration of IMUs under the presented conditions but also the analysis of such impacts on positioning algorithms, as well as the integration of temperature stress in the current characterization.

REFERENCES

- [1] D. G. Pascual, P. Daponte, and U. Kumar, *Handbook of Industry 4.0 and SMART Systems*. Boca Raton, FL, USA: CRC Press, 2020.
- [2] G. D'Emilia, A. Gaspari, and E. Natale, "Mechatronics applications of measurements for smart manufacturing in an industry 4.0 scenario," *IEEE Instrum. Meas. Mag.*, vol. 22, no. 2, pp. 35–43, Apr. 2019.
- [3] G. D'Emilia, A. Gaspari, D. Lancione, and E. Natale, "Prediction of the remaining useful life of mechatronic systems, using internal sensors," in *Proc. IEEE Int. Workshop Metrology Ind. 4.0 IoT*, Jun. 2020, pp. 75–79.
- [4] M. Rezamand, M. Kordestani, R. Cariveau, D. S.-K. Ting, M. E. Orchard, and M. Saif, "Critical wind turbine components prognostics: A comprehensive review," *IEEE Trans. Instrum. Meas.*, vol. 69, no. 12, pp. 9306–9328, Dec. 2020.
- [5] K. Cai, T. Qu, H. Chen, B. Gao, and N. Bian, "Low-cost hybrid multisensor fusion method and implementation for production intelligent vehicles," *IEEE Trans. Instrum. Meas.*, vol. 71, pp. 1–16, 2022.
- [6] H. Guo, Q. Meng, D. Cao, H. Chen, J. Liu, and B. Shang, "Vehicle trajectory prediction method coupled with ego vehicle motion trend under dual attention mechanism," *IEEE Trans. Instrum. Meas.*, vol. 71, pp. 1–16, 2022.
- [7] J. Zhang, Y. Liu, Y. Li, and J. Yu, "A unified framework for automobile instrument detection system," *IEEE Trans. Instrum. Meas.*, vol. 71, pp. 1–11, 2022.
- [8] Y. Cai, Z. Lu, H. Wang, L. Chen, and Y. Li, "A lightweight feature map creation method for intelligent vehicle localization in urban road environments," *IEEE Trans. Instrum. Meas.*, vol. 71, pp. 1–15, 2022.
- [9] C. Zhang et al., "Robust-FusionNet: Deep multimodal sensor fusion for 3-D object detection under severe weather conditions," *IEEE Trans. Instrum. Meas.*, vol. 71, pp. 1–13, 2022.
- [10] D. Capriglione et al., "Characterization of inertial measurement units under environmental stress screening," in *Proc. IEEE Int. Instrum. Meas. Technol. Conf.*, May 2020, pp. 1–6.
- [11] G. Andria, F. Attivissimo, A. Di Nisio, A. M. L. Lanzolla, and A. Pellegrino, "Development of an automotive data acquisition platform for analysis of driving behavior," *Measurement*, vol. 93, pp. 278–287, Nov. 2016.
- [12] W. Sun, D. Wang, L. Xu, and L. Xu, "MEMS-based rotary strapdown inertial navigation system," *Measurement*, vol. 46, no. 8, pp. 2585–2596, Oct. 2013.
- [13] P. Mohankumar, J. Ajayan, R. Yasodharan, P. Devendran, and R. Sambasivam, "A review of micromachined sensors for automotive applications," *Measurement*, vol. 140, pp. 305–322, Jul. 2019.
- [14] D. Capriglione et al., "Experimental analysis of IMU under vibration," in *Proc. 16th IMEKO TC10 Conf., 'Test., Diagnostics Inspection Comprehensive Value Chain Quality Safety'*, 2019, pp. 26–31.
- [15] Y. Tian, T. An, F. Qin, Y. Gong, Y. Dai, and Y. Chen, "Stress analysis of automotive IGBT module under vibration load," in *Proc. 23rd Int. Conf. Electron. Packag. Technol. (ICEPT)*, Aug. 2022, pp. 1–4.
- [16] X. Liu, C. Zhang, X. Ling, and X. Shi, "Research on the transient vibration characteristics of vehicle transmission system," in *Proc. Int. Conf. Electron., Circuits Inf. Eng. (ECIE)*, Jan. 2021, pp. 112–117.
- [17] D. Capriglione et al., "Performance analysis of MEMS-based inertial measurement units in terrestrial vehicles," *Measurement*, vol. 186, Dec. 2021, Art. no. 110237.
- [18] R. Höhne, K. Meier, A. Dasgupta, D. Leslie, and K. Bock, "Improved damage modeling for solder joints under combined vibration and temperature cycling loading," in *Proc. IEEE 71st Electron. Compon. Technol. Conf. (ECTC)*, Jun. 2021, pp. 1353–1358.
- [19] W. Li et al., "A study on performance characterization considering six-degree-of-freedom vibration stress and aging stress for electric vehicle battery under driving conditions," *IEEE Access*, vol. 7, pp. 112180–112190, 2019.
- [20] E. E. Aktakka, J. Woo, and K. Najafi, "On-chip characterization of scale-factor of a MEMS gyroscope via a micro calibration platform," in *Proc. IEEE Int. Symp. Inertial Sensors Syst. (INERTIAL)*, Mar. 2017, pp. 1–4.
- [21] S. Ailneni et al., "Characterization of MEMS based inertial measurement unit," in *Proc. Int. Conf. Range Technol. (ICORT)*, Feb. 2019, pp. 1–5.
- [22] R. Li, Z. Mohammed, M. Rasras, I. M. Elfadel, and D. Choi, "Design, modelling and characterization of comb drive MEMS gap-changeable differential capacitive accelerometer," *Measurement*, vol. 169, Feb. 2021, Art. no. 108377.
- [23] R. Holm, H. Schou, H. R. Petersen, and M. Horntvedt, "Behavioral performance during vibration and shock for a tactical grade IMU," in *Proc. DGON Inertial Sensors Syst. (ISS)*, Sep. 2018, pp. 1–19.
- [24] D. Capriglione et al., "Experimental analysis of filtering algorithms for IMU-based applications under vibrations," *IEEE Trans. Instrum. Meas.*, vol. 70, pp. 1–10, 2021.
- [25] D. Capriglione et al., "Development of a test plan and a testbed for performance analysis of MEMS-based IMUs under vibration conditions," *Measurement*, vol. 158, Jul. 2020, Art. no. 107734.
- [26] G. Betta et al., "Stress testing for performance analysis of orientation estimation algorithms," *IEEE Trans. Instrum. Meas.*, vol. 71, pp. 1–12, 2022.
- [27] Y. Yuksel, N. El-Sheimy, and A. Noureldin, "Error modeling and characterization of environmental effects for low cost inertial MEMS units," in *Proc. IEEE/ION Position, Location Navigat. Symp.*, May 2010, pp. 598–612.
- [28] X. Yuan, S. Yu, S. Zhang, C. Liu, and S. Liu, "Modeling and analysis of wearable low-cost MEMS inertial measurement units," in *Proc. 15th Int. Conf. Electron. Packag. Technol.*, Aug. 2014, pp. 542–546.
- [29] *Road Vehicle—Environmental Conditions and Testing for Electrical and Electronic Equipment—Part 3: Mechanical Loads*, Standard IOS 16750-3, 2003.
- [30] *Environmental Testing—Part 2: Tests—Test Fh: Vibration, Broadband Random and Guidance*, Standard IEC 60068-2-64, 2008.

- [31] *Failure Mechanism Based Stress Test Qualification for Integrated Circuit*, Automotive Electronics Council, USA, 2014.
- [32] *Environmental Engineering (EE); Environmental Conditions and Environmental Tests for Telecommunications Equipment; Part 2-5: Specification of Environmental Tests; Ground Vehicle Installations*, document ETSI EN 300 019-2-5, 2002.
- [33] *iNEMO Inertial Module: 3D Accelerometer, 3D Gyroscope, 3D Magnetometer*, ST Microelectronics, Geneva, Switzerland, 2015.



Gabriele Patrizi (Member, IEEE) received the master's degree (cum laude) in electronic engineering and the Ph.D. degree in industrial and reliability engineering from the University of Florence, Florence, Italy, in 2018 and 2022, respectively.

In 2022, he joined the Institute of Electronic Packaging Technology (IAVT), Dresden Technical University, Dresden, Germany, as a Visiting Post-Doctoral Researcher. He is currently a Post-Doctoral Research Fellow of Instrumentation and Measurement and an Adjunct Lecturer of Electric

Measurements with the University of Florence. His research interests include life cycle reliability, condition monitoring for fault diagnosis of electronics, data-driven prognostic and health management, and instrumentation and measurement for reliability analysis.

Dr. Patrizi received the "2023 Best Dissertation Award" from the IEEE IMS. He has been an Associate Editor of IEEE TRANSACTIONS ON INSTRUMENTATION AND MEASUREMENT (TIM) since 2023.



Marco Carratù (Member, IEEE) received the M.S. degree in electronic engineering and the Ph.D. degree from the University of Salerno, Fisciano, Italy, in 2015 and 2019, respectively.

He is currently an Assistant Professor of Electronic Measurements with the Department of Industrial Engineering, University of Salerno. His current research interests include instrument fault detection and isolation, sensor data fusion, digital signal processing for advanced instrumentation, artificial intelligence (AI) for instrumentation and measurement, and real-time embedded systems.



Lorenzo Ciani (Senior Member, IEEE) received the M.S. degree in electronic engineering and the Ph.D. degree in industrial and reliability engineering from the University of Florence, Florence, Italy, in 2005 and 2009, respectively.

He is currently an Associate Professor with the Department of Information Engineering, University of Florence. He has authored or coauthored more than 190 peer-reviewed journal articles and conference papers. His current research interests include system reliability, availability, maintainability, and safety, reliability evaluation test and analysis for electronic systems and devices, fault detection and diagnosis, and electrical and electronic instrumentation and measurement.

Dr. Ciani is a member of the IEEE IMS TC-32 Fault Tolerant Measurement Systems. He is the Associate Editor-in-Chief of the IEEE TRANSACTIONS ON INSTRUMENTATION AND MEASUREMENT and an Associate Editor of the IEEE ACCESS. He was a recipient of the 2015 IEEE I&M Outstanding Young Engineer Award for "his contribution to the advancement of instrumentation and measurement in the field of reliability analysis."



Paolo Sommella (Member, IEEE) was born in Salerno, Italy, in 1979. He received the M.S. degree in electronic engineering and the Ph.D. degree in information engineering from the University of Salerno, Fisciano, Italy, in 2004 and 2008, respectively.

In 2015, he joined the Department of Industrial Engineering (DIIn), University of Salerno, as an Assistant Professor of Electrical and Electronic Measurements. His main interests are instrument fault detection and isolation, measurement in software engineering, and biomedical image processing.



Marcantonio Catelani (Member, IEEE) received the M.S. degree in electronic engineering from the University of Florence, Florence, Italy, in 1984.

He is currently with the Department of Information Engineering, University of Florence. Strictly correlated with reliability, availability, maintainability, and safety (RAMS) are the fields of interest of both the fault diagnosis and reliability testing for components and equipment. In particular, the research activity concerns the development of test profiles used both for the characterization and the evaluation

of reliability performance and, at the same time, the development of new degradation models able to estimate the life cycle of electronic components. His current research interests include the development of automatic measurement system, the characterization of A/D converters, quality control and related statistical methods, and RAMS context.



Antonio Pietrosanto (Senior Member, IEEE) has been a Full Professor of Instrumentation and Measurement with the University of Salerno, Fisciano, Italy, since 2001. He is the Founder of three spin-off companies of the University of Salerno: "SPRING OFF," "Metering Research," and "Hippocratica Imaging." He has coauthored more than 150 articles in international journals and conference proceedings. His main research activities are in the fields of instrument fault detection and isolation (IFDIA), sensors, wireless sensor networks (WSNs), real-time measurements, embedded systems, metrological characterization of measurement software, advanced system for food quality inspection, and image-based measurements.

Mr. Pietrosanto is the today President of the Didactic Board of Electronic Engineering of UniSA.